Check for updates

View Article Online
View Journal

Chemical Science

Accepted Manuscript

This article can be cited before page numbers have been issued, to do this please use: X. Li, Q. Li, B. Chen, M. Wang, C. Yan, S. Jana, Z. Liao, Z. Li, D. Gao and G. Wang, *Chem. Sci.*, 2025, DOI: 10.1039/D5SC04541J.

This is an Accepted Manuscript, which has been through the Royal Society of Chemistry peer review process and has been accepted for publication.

Accepted Manuscripts are published online shortly after acceptance, before technical editing, formatting and proof reading. Using this free service, authors can make their results available to the community, in citable form, before we publish the edited article. We will replace this Accepted Manuscript with the edited and formatted Advance Article as soon as it is available.

You can find more information about Accepted Manuscripts in the Information for Authors.

Please note that technical editing may introduce minor changes to the text and/or graphics, which may alter content. The journal's standard Terms & Conditions and the Ethical guidelines still apply. In no event shall the Royal Society of Chemistry be held responsible for any errors or omissions in this Accepted Manuscript or any consequences arising from the use of any information it contains.

ROYAL SOCIETY OF CHEMISTRY

rsc.li/chemical-science

Please do not adjust margins

View Article Online
DOI: 10.1039/D5SC04541J

Received 00th January 20xx,
Accepted 00th January 20xx

DOI: 10.1039/x0xx00000x

Regulating metal-oxygen covalency in reconstructed sulfurized high-entropy perovskite to activate and stabilize lattice oxygen for oxygen evolution reaction

Xiang Li,[a,b] Qiuju Li,[c] Bingyu Chen,[d] Mengna Wang,[a,b] Chuanchuan Yan,[a,d] Subhajit Jana,[e] Ziqi Liao,[a,d] Zhenyu Li,[a,*] Dunfeng Gao,[a] Guoxiong Wang[a,*]

Switching adsorbate evolution mechanism (AEM) to lattice oxygen mechanism (LOM) can break the theoretical limit of catalytic activity for oxygen evolution reaction (OER). However, LOM-dominated catalysts are difficult to simultaneously obtain high activity and stability because of their trade-off relationship. Here, we report a reconstructed sulfurized high-entropy perovskite (S-LaNiFeCoCrMnO$_3$) possesses excellent activity with an overpotential of 165 mV and has a high catalytic stability for 1800 h at 10 mA/cm^2 toward the OER. Furthermore, the S-LaNiFeCoMnCrO$_3$ as anode catalyst in anion exchange membrane water electrolyzer exhibits a high current density of 5.8 A/cm^2 at the cell voltage of 2.0 V. *On line* differential electrochemical mass spectrometry results suggest that the increased reactivity of lattice oxygen in reconstructed S-LaNiFeCoCrMnO$_3$ facilitates the enhancement of OER activity. X-ray absorption near-edge structure and *in situ* Raman spectroscopy results reveal that the local Ni-S bond in the sulfurized layer on the surface of S-LaNiFeCoCrMnO$_3$ drives the generation of Fe-NiOOH active phase with NiO$_2$ subunit layer and high-valent Ni^{4+} species. Furthermore, strong covalent Ni-O and weak covalent Fe-O bonds in the Fe-NiOOH active phase play a critical role of activating and stabilizing lattice oxygen, thus breaking the activity-stability trade-off relationship for the LOM.

Open Access Article. Published on 17 2025. Downloaded on 23/09/25 16:31:42.
This article is licensed under a Creative Commons Attribution 3.0 Unported Licence.

Chemical Science Accepted Manuscript

Introduction

The growing global energy demand has accelerated the depletion of fossil fuels and generated serious environmental problems.[1,2] Hydrogen as a typically clean and sustainable energy source is an important exploration direction for the future energy revolution that mankind should consider and conduct.[3,4] Hydrogen production by anion exchange membrane water electrolyzer (AEMWE) has attracted much attention because it allows the application of nonprecious metal-based catalysts without affecting the catalytic activity and stability of oxygen evolution reaction (OER).[5,6] However, the slow kinetics for anodic OER leads to a high overpotential and excessive energy consumption, severely limiting the industrialized process for the AEMWE.[7,8] Therefore, exploring a high-performance OER catalyst is crucial for overcoming the high energy consumption in the AEMWE, and its first task is the in-depth understanding of the catalytic mechanism for the OER. In general, for the conventional adsorbate evolution mechanism (AEM), the adsorption strength of various intermediate adsorbents involved in the OER is highly proportional to their catalytic activity, and they also undergo a coordinated electron transfer process during electrocatalysis, resulting in a theoretical limit for the overpotential of 0.37 V.[9,10] Unlike the AEM, the lattice oxygen mechanism (LOM) is a catalytic pathway of uncoordinated proton-electron transfer process for directly coupling O-O bond.[11,12] Although the LOM-dominated catalysts breaks the theoretical overpotential limit of the AEM for the OER, it is still difficult to obtain satisfactory catalytic stability in the three-electrode system. Furthermore, it is more difficult to adapt the industrial water electrolysis operated in the AEMWE.

So far, several oxygen-containing OER catalysts, such as borates, spinels, hydroxides, and perovskites have been identified to conform to the LOM toward OER.[13-15] Among the above catalysts, due to the structural compatibility of various elements in the B position of perovskite oxides, high-entropy perovskite as an attractive candidate has emerged toward the OER.[16] Although the increased reactivity of lattice oxygen in high-entropy perovskite triggers the enhancement of catalytic activity toward the OER, the structural collapse by leaching metal cations during the electrocatalytic process results in poor stability. Furthermore, it is still difficult to be applied in AEMWE because of the low conductivity.[17] Therefore, it is crucial to regulate the lattice oxygen reactivity as well as solve the trade-off relationship between catalytic activity and stability for LOM in high entropy perovskite. In addition, theoretical calculations and *in situ* spectroscopy studies have revealed that the oxide/hydroxide/oxyhydroxide formed on the catalyst surface by surface reconstruction during OER facilitates the activation of lattice oxygen and plays a key role in LOM pathway.[18,19] While the previous works have proved that self-restructuring during the OER is an effective way to obtain highly active LOM-based catalysts, the influences of

[a]*State Key Laboratory of Catalysis Energy, Dalian National Laboratory for Clean Energy iChEM (Collaborative Innovation Center of Chemistry for Energy Materials), Dalian Institute of Chemical Physics Chinese Academy of Sciences, Dalian 116023, China*
[b]*Department of Chemistry, College of Basic Medicine, Third Military Medical University (Army Medical University), Chongqing 400038, China*
[c]*Dalian Jiaotong University, Dalian 116028, China*
[d]*University of Chinese Academy of Sciences, Beijing 100049, China*
[e]*Department of Mechanical and Mechatronics Engineering, Waterloo Institute for Nanotechnology, Materials Interfaces Foundry, University of Waterloo, Waterloo, Ontario N2L3G1, Canada*

Please do not adjust margins

View Article Online
DOI: 10.1039/D5SC04541J

composition and structure of pre-catalyst on the catalytic activity have not been well investigated.[20] This not only resulted in an incomplete understanding of LOM, but also hindered the exploration and rational design of efficient OER catalysts. Regulating the covalency of metal-oxygen bond in the LOM-based catalyst is favorable to the redox of lattice oxygen during the OER. Doping S with high electronegativity (2.58) not only increases the ion conductivity/oxygen ion diffusion rate on the perovskite surface, but also enhances the covalency of metal-O bond, thus promoting the reactivity of lattice oxygen.[21] Furthermore, introducing sulfurized layer on the surface can facilitate surface reconstruction and significantly promote the generation of the active phase for oxide/hydroxide/oxyhydroxide on high-entropy perovskite surface during the OER.[22]

Herein, a sulfurized high-entropy perovskite (S-$LaNiFeCoCrMnO_3$) catalyst was prepared by co-precipitation method and subsequent chemical vapor deposition process. The reconstructed S-$LaNiFeCoCrMnO_3$ as an OER catalyst exhibited an overpotential of 165 mV and excellent catalytic stability for 1800 h. Furthermore, the reconstructed S-$LaNiFeCoCrMnO_3$ as an anode catalyst in the AEMWE displayed a current density of 1.0 A/cm^2 and 5.8 A/cm^2 at the cell voltage of 1.61 V and 2.0 V, respectively. Combining X-ray absorption near-edge structure spectroscopy (XANES), *in situ* Raman spectroscopy, and cyclic voltammogram (CV) results demonstrated S atoms, which mainly coordinated with Ni atom to form Ni-S bond in the S-$LaNiFeCoCrMnO_3$ pre-catalyst, were partially leached, increasing coordinate numbers (CNs) of Ni-O bond, promoting the adsorption of the oxygen-containing intermediates, and thus facilitating the surface reconstruction of catalyst during the OER to *in situ* form Fe-NiOOH active phase with NiO_2 subunit layer and Ni^{4+} species. *On line* differential electrochemical mass spectrometry, TMAOH-distributed experiments test, and density functional theory (DFT) calculation results reveal that Fe-NiOOH active phase with NiO_2 subunit layer and Ni^{4+} species formed on reconstructed S-$LaNiFeCoCrMnO_3$ catalyst enhances the reactivity of lattice oxygen, thus improving the OER activity. Furthermore, strong covalent Ni-O and weak covalent Fe-O bonds in the Fe-NiOOH active phase played a critical role of activating and stabilizing lattice oxygen, thus breaking the trade-off relationship between activity and stability for the LOM.

Results and discussion

Synthesis and characterizations of S-$LaNiFeCoCrMnO_3$

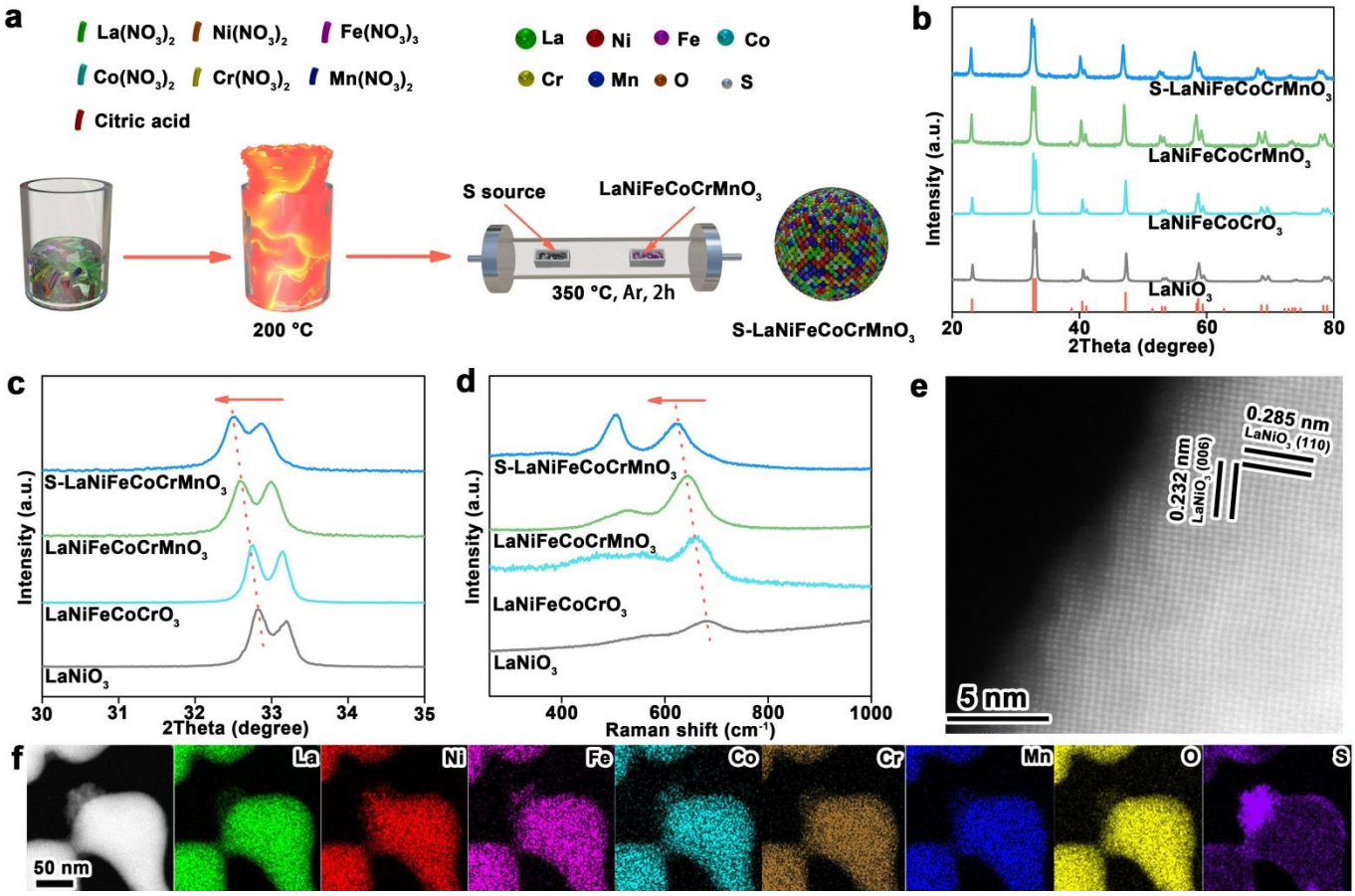

Fig. 1 Synthesis and characterizations of S-$LaNiFeCoCrMnO_3$ catalyst. (a) Synthesis schematic of S-$LaNiFeCoCrMnO_3$ catalyst. (b-c) XRD and corresponding magnified patterns of $LaNiO_3$, $LaNiFeCoCrO_3$, $LaNiFeCoCrMnO_3$, and S-$LaNiFeCoCrMnO_3$ catalysts. (d) Raman spectra of $LaNiO_3$, $LaNiFeCoCrO_3$, $LaNiFeCoCrMnO_3$, and S-$LaNiFeCoCrMnO_3$ catalysts. (e) HRTEM image of S-$LaNiFeCoCrMnO_3$ catalyst. (f) STEM image and corresponding elemental maps of S-$LaNiFeCoCrMnO_3$ catalyst.

Open Access Article. Published on 17 2025. Downloaded on 23/09/25 16:31:42.
This article is licensed under a Creative Commons Attribution 3.0 Unported Licence.

Chemical Science Accepted Manuscript

This journal is © The Royal Society of Chemistry 20xx

Please do not adjust margins
View Article Online
DOI: 10.1039/D5SC04541J

Open Access Article. Published on 17 2025. Downloaded on 23/09/25 16:31:42.
This article is licensed under a Creative Commons Attribution 3.0 Unported Licence.

Sulfurized high-entropy perovskite catalyst (S-$LaNiFeCoCrMnO_3$) was synthesized through a two-step method (the detailed procedure was provided in the experimental section): (1) Using the co-precipitation method to prepare high-entropy perovskite oxide catalyst ($LaNiFeCoCrMnO_3$); (2) Subsequently, S-$LaNiFeCoCrMnO_3$ was obtained using chemical vapor deposition method to conduct the surface sulfuration of as-prepared $LaNiFeCoCrMnO_3$ (**Fig. 1a**). X-ray diffraction (XRD) patterns demonstrate the precise synthesis of S-$LaNiFeCoCrMnO_3$ with the single-phase hexagonal structure (**Fig. 1b**). The diffraction peak located at ~33° for S-$LaNiFeCoCrMnO_3$ shifts toward a low angle compared to $LaNiO_3$, $LaNiFeCoCrO_3$, and $LaNiFeCoCrMnO_3$ in the magnified XRD patterns (**Fig. 1c**), indicative of the lattice distortions caused by the differences in atomic diameters of the six elements.[23] The Raman spectra at ~690 cm^{-1}, representing B_{1g} stretching vibration of octahedron (NiO_6), showed a negatively shifted trend as the increase of the elements in crystal structure for $LaNiO_3$, $LaNiFeCoCrO_3$, $LaNiFeCoCrMnO_3$, and S-$LaNiFeCoCrMnO_3$ catalysts (**Fig. 1d**), indicating the enhanced degree of lattice distortions.[24] Besides, the strong Raman peak, appeared at ~500 cm^{-1}, is ascribed to NiO_6 octahedron for S-$LaNiFeCoCrMnO_3$. The introduction of S in S-$LaNiFeCoCrMnO_3$ leads to the increased Ni^{3+} ratio, thus enhancing Raman peak intensity of NiO_6. Transmission electron microscope (TEM) and scanning electron microscopy (SEM) images exhibit that S-$LaNiFeCoCrMnO_3$ maintains a similar morphology of nanoparticles with the size of 100~200 nm compared with $LaNiO_3$, $LaNiFeCoCrO_3$, and $LaNiFeCoCrMnO_3$ (**Figs. S1-S2**). Different from $LaNiO_3$, $LaNiFeCoCrO_3$, and $LaNiFeCoCrMnO_3$, a rough surface can be observed for S-$LaNiFeCoCrMnO_3$. High-resolution TEM (HRTEM) displays the measured interplanar distances of 0.232 nm and 0.285 nm, assigning to the (006) and (110) crystal facets for S-$LaNiFeCoCrMnO_3$, respectively (**Fig. 1e**). Besides, the (110) interplanar distance in S-$LaNiFeCoCrMnO_3$ is larger than that in $LaNiO_3$, $LaNiFeCoCrO_3$, and $LaNiFeCoCrMnO_3$ (**Fig. 1e and Fig. S3**), demonstrating the lattice expansion. STEM and SEM elemental maps show that La, Ni, Fe, Co, Cr, Mn, and O elements are uniformly distributed in S-$LaNiFeCoCrMnO_3$ while S element mainly distributes on its surface overlayer, demonstrating that the thin sulfurized layer forms on the surface of S-$LaNiFeCoCrMnO_3$. (**Fig. 1f** and **Fig. S4**).

OER Performance of S-$LaNiFeCoCrMnO_3$

We conducted the electrochemical measurements to evaluate the catalytic performance toward the OER in 1.0 M KOH using a standard three-electrode system. Linear sweep voltammetry (LSV) normalized by electrode area in **Fig. 2a** displays that S-$LaNiFeCoCrMnO_3$ can obtain a current density of 10 mA/cm^2 at an overpotential of 165 mV, outperforming the $LaNiO_3$ (389 mV), $LaNiFeCoCrO_3$ (329 mV), and $LaNiFeCoCrMnO_3$ (315 mV). Impressively, S-$LaNiFeCoCrMnO_3$ only needs an overpotential of 195 mV and 251 mV to gain a high current density of 100 and 500 mA/cm^2, respectively. The electrochemical active surface area (ECSA) of S-$LaNiFeCoCrMnO_3$ is significantly higher than that of $LaNiO_3$, $LaNiFeCoCrO_3$, and $LaNiFeCoCrMnO_3$, demonstrating the exposure of more active sites after sulfuration (**Figs. S5-S6**). Furthermore, the ECSA-normalized catalytic performance exhibits an increased trend in the order of $LaNiO_3$, $LaNiFeCoCrO_3$, $LaNiFeCoCrMnO_3$, and S-$LaNiFeCoCrMnO_3$, confirming the same trend as their geometric activities (**Fig. 2b** and **Fig. S7**). S-$LaNiFeCoCrMnO_3$ possesses superior activity when the reaction time and temperature in the synthesis procedure were set to 2 h and 350 °C, respectively (**Figs. S8-S11**). As shown in **Fig. 2c**, S-$LaNiFeCoCrMnO_3$ has the smallest Tafel slope of 61.3 mV/dec compared to $LaNiO_3$ (82.3 mV/dec), $LaNiFeCoCrO_3$ (86.7 mV/dec), and $LaNiFeCoCrMnO_3$ (146.0 mV/dec), accelerating the reaction kinetic toward the OER. [25,26] The electrochemical impedance spectroscopy (EIS) test reveals that electron-transfer resistance of S-$LaNiFeCoCrMnO_3$ is lower than that of $LaNiO_3$, $LaNiFeCoCrO_3$, and $LaNiFeCoCrMnO_3$, demonstrating fast charge-transfer capacity at the interface between catalyst and electrolyte for facilitating the reaction kinetics toward the OER (**Fig. S12**).[27] In addition, S-$LaNiFeCoCrMnO_3$ exhibits a Faradaic efficiency approaching 100% (**Fig. S13**).

The stability of catalyst is an important index for the OER. As shown in **Fig. 2d**, the overpotentials at 10 mA/cm^2 toward the OER for $LaNiO_3$ and $LaNiFeCoCrO_3$ display a pronounced increase before 300 h. Compared with $LaNiO_3$ and $LaNiFeCoCrO_3$, the overpotential of $LaNiFeCoCrMnO_3$ exhibits less increase before 300 h, but shows a slight increase after ~1000 h, demonstrating that the regulation of entropy in pre-catalysts can enhance the stability toward OER. In particular, the S-$LaNiFeCoCrMnO_3$ maintains excellent stability for 1800 h (75 days), confirming that the sulfurized overlayer formed on S-$LaNiFeCoCrMnO_3$ further enhances the stability of the catalyst. As for S-$LaNiFeCoCrMnO_3$, the activity is increased at the initial stage before 600 h during stability test, suggesting the occurrence of surface reconstruction. Besides, S-$LaNiFeCoCrMnO_3$ exhibits a more prolonged surface reconstruction than that of $LaNiO_3$, $LaNiFeCoCrO_3$, and $LaNiFeCoCrMnO_3$, suggesting that the existence of sulfide layer promotes the surface reconstruction. After surface reconstruction, the activity of S-$LaNiFeCoCrMnO_3$ keep stable, implying that the lattice oxygen participates in OER. The XRD pattern and SEM image after stability test display that the morphology, phase structure, and elemental distribution are unchanged, demonstrating excellent structural stability of S-$LaNiFeCoCrMnO_3$ (**Figs. S14-16**). Furthermore, inductively coupled plasma-optical emission spectrometry (ICP-OES) result reveals that the La, Ni, Fe, Co, Cr, and Mn elements did not dissolve out obviously, while S precipitated obviously for S-$LaNiFeCoCrMnO_3$ catalyst during OER (**Fig. S17**). S leaching in S-

Chemical Science Accepted Manuscript

Please do not adjust margins

View Article Online
DOI: 10.1039/D5SC04541J

Open Access Article. Published on 17 2025. Downloaded on 23/09/25 16:31:42.
This article is licensed under a Creative Commons Attribution 3.0 Unported Licence.

$LaNiFeCoCrMnO_3$ during OER increases coordinate numbers (CNs) of Ni-O bond, promoting the adsorption of the oxygen-containing intermediates, and thus facilitating the surface reconstruction of catalyst during the OER to *in situ* form oxyhydroxide active phase. Considering the low overpotential and high stability, the S-$LaNiFeCoCrMnO_3$ possesses higher OER performance than the most previously reported catalysts, including perovskites, sulfides, and even other high-entropy materials (**Table S1** and **Fig. 2e**).[28-30]

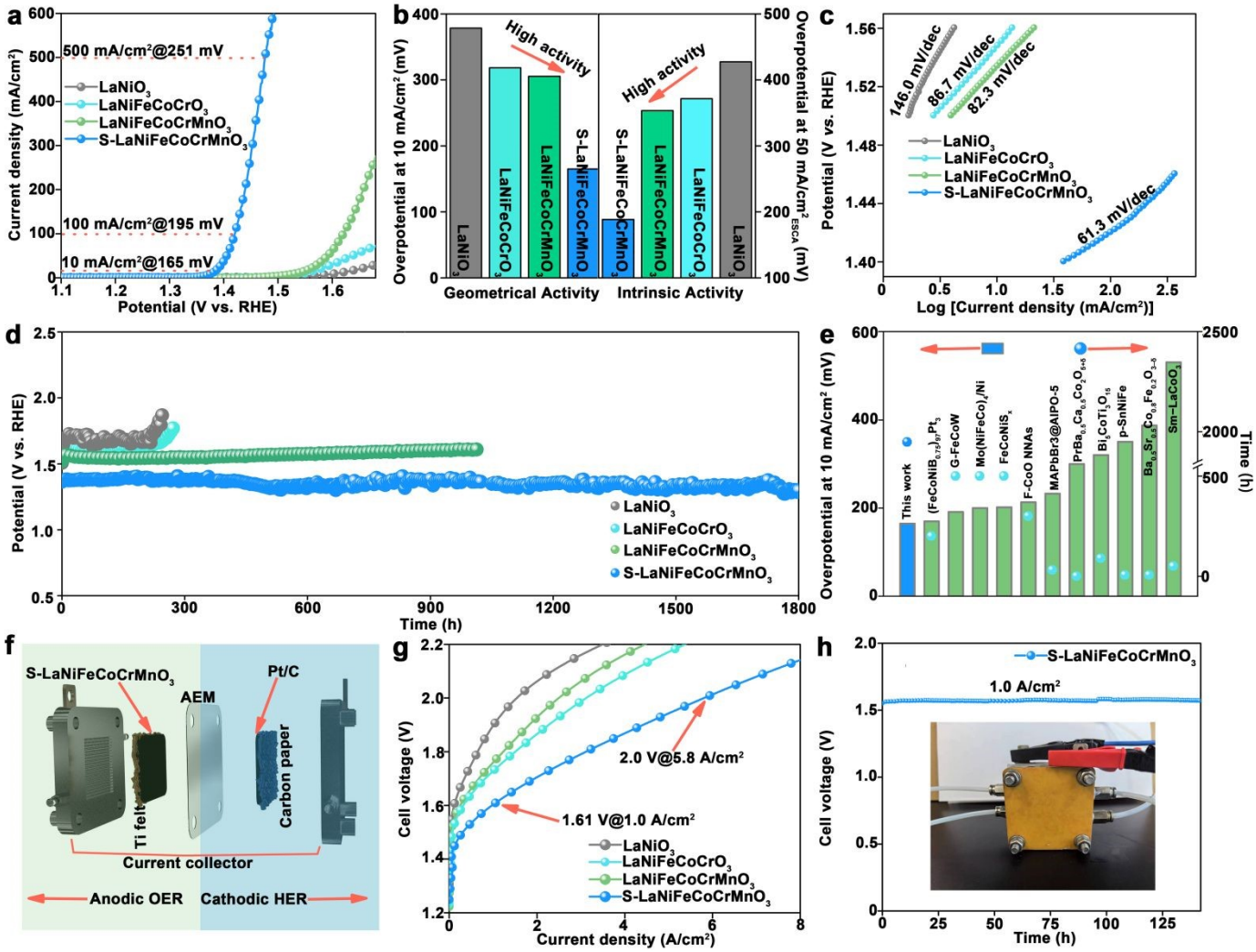

Fig. 2 Electrocatalytic performance evaluation of S-$LaNiFeCoCrMnO_3$ catalyst toward the OER in 1.0 M KOH solution. (a) LSV curves of $LaNiO_3$, $LaNiFeCoCrO_3$, $LaNiFeCoCrMnO_3$, and S-$LaNiFeCoCrMnO_3$ catalysts. (b) Comparison of geometric and ECSA-normalized activity for $LaNiO_3$, $LaNiFeCoCrO_3$, $LaNiFeCoCrMnO_3$, and S-$LaNiFeCoCrMnO_3$ catalysts. (c) Tafel slopes of $LaNiO_3$, $LaNiFeCoCrO_3$, $LaNiFeCoCrMnO_3$, and S-$LaNiFeCoCrMnO_3$ catalysts. (d) Chronopotentiometric curves of $LaNiO_3$, $LaNiFeCoCrO_3$, $LaNiFeCoCrMnO_3$, and S-$LaNiFeCoCrMnO_3$ catalysts at 10 mA/cm². (e) Comparison of S-$LaNiFeCoCrMnO_3$ and previously reported catalysts for perovskite oxides and sulfides. (f) Schematic diagram to illustrate the anodic oxygen evolution and cathodic hydrogen evolution in AEMWE. (g) Polarization curves of $LaNiO_3$, $LaNiFeCoCrO_3$, $LaNiFeCoCrMnO_3$, and S-$LaNiFeCoCrMnO_3$ as anode catalysts in anion exchange membrane water electrolyzer. (h) Chronopotentiometric curve of S-$LaNiFeCoCrMnO_3$ as an anode catalyst at 1.0 A/cm² in AEMWE.

Chemical Science Accepted Manuscript

This journal is © The Royal Society of Chemistry 20xx

Please do not adjust margins

View Article Online
DOI: 10.1039/D5SC04940

To evaluate the industrial prospect of the S-LaNiFeCoCrMnO$_3$ catalyst, we conducted the AEMWE measurements. The S-LaNiFeCoCrMnO$_3$ as an anode catalyst was coated on the side of Ti felt gas diffusion layer (GDL), while commercial Pt/C as a cathode catalyst was coated on carbon paper GDL. Subsequently, the Ti felt GDL with S-LaNiFeCoCrMnO$_3$ and carbon paper GDL with Pt/C were pressed on both sides of AEM, respectively, thus establishing membrane electrode assembly (MEA) for AEMWE (**Fig. 2f**). SEM image (**Fig. S18**) and corresponding cross-sectional SEM elemental maps (**Fig. S19**) illustrates the thickness of catalyst layer on S-LaNiFeCoCrMnO$_3$-coated GDL is ~10 μm. Polarization curves of AEMWEs measured in 1.0 M KOH at 80 °C exhibit that S-LaNiFeCoCrMnO$_3$ as an anode catalyst only requires a cell voltage of 1.61 V to deliver a current density of 1.0 A/cm^2, outperforming LaNiFeCoCrMnO$_3$ (1.73 V), LaNiFeCoCrO$_3$ (1.76 V), LaNiO$_3$ (1.89 V), and previously reported representative catalysts (**Fig. 2g** and **Table S2**). Moreover, the high current density of 5.8 A/cm^2 can be obtained at the cell voltage of 2.0 V, suggesting the industrial prospect of S-LaNiFeCoCrMnO$_3$. The AEMWE using S-LaNiFeCoCrMnO$_3$ anode catalyst can steadily operate at a current density of 1.0 A/cm^2 for over 140 h, suggesting excellent catalytic stability under the industrial conditions (**Fig. 2h**). The SEM image and corresponding elemental maps reveal that the catalyst layer still integrally existed on the AEM surface after stability test, suggesting the anti-corrosion capacity (**Fig. S20**).

Revealing active phase for S-LaNiFeCoCrMnO$_3$ catalyst

To reveal the catalytic active phase of S-LaNiFeCoCrMnO$_3$, X-ray photoelectron spectroscopy (XPS), HAADF-STEM, and *in situ* Raman spectroscopy measurements were carried out. HAADF-STEM image shows that the surface yields an amorphous oxide layer with a thickness of 2 nm (**Fig. 3a**), suggesting the reconstruction of S-LaNiFeCoCrMnO$_3$ surface after the OER. HAADF-STEM image also displays that the atomic arrange and the resultant fast Fourier transform (FFT) pattern of S-LaNiFeCoCrMnO$_3$ catalyst after stability test are consistent with the corresponding theoretical result, indicating that it still maintains the original structure of bulk phase (**Fig. 3b** and **Figs. 21-22**). Atomic-level line scanning EDX spectra from bulk to surface show that the amorphous oxide layer on S-LaNiFeCoCrMnO$_3$ surface mainly contains Ni, Fe, and O elements (**Fig. S23** and **Fig. 3c**).

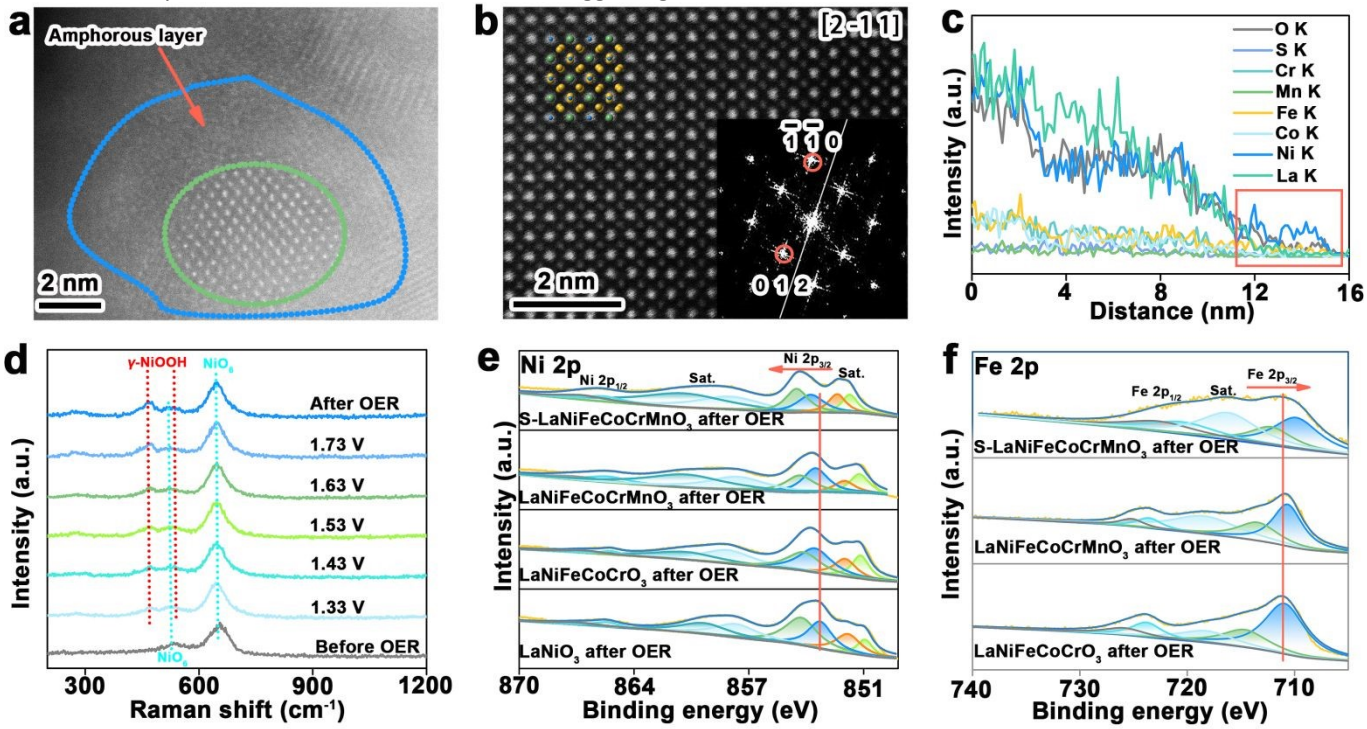

Fig. 3 Recognition of the active phase for S-LaNiFeCoCrMnO$_3$ catalyst toward the OER. (a) High-resolution HAADF-STEM image of S-LaNiFeCoCrMnO$_3$ catalyst after stability test. (b) Magnified high-resolution HAADF-STEM image of S-LaNiFeCoCrMnO$_3$ catalyst after stability test. Inset shows the corresponding FFT image. (c) Atom-level line scanning EDX spectra of S-LaNiFeCoCrMnO$_3$ catalyst after stability test. (d) In situ Raman spectra of S-LaNiFeCoCrMnO$_3$ catalyst. (e) Ni 2p XPS spectra of LaNiO$_3$, LaNiFeCoCrO$_3$, LaNiFeCoCrMnO$_3$, and S-LaNiFeCoCrMnO$_3$ catalysts after stability test. (f) Fe 2p XPS spectra of LaNiFeCoCrO$_3$, LaNiFeCoCrMnO$_3$, and S-LaNiFeCoCrMnO$_3$ catalysts after stability test.

In situ Raman spectra for LaNiO$_3$, LaNiFeCoCrO$_3$, LaNiFeCoCrMnO$_3$, and S-LaNiFeCoCrMnO$_3$ catalysts are shown in **Fig. 3d** and **Fig. S24**. For LaNiO$_3$, LaNiFeCoCrO$_3$, and LaNiFeCoCrMnO$_3$ catalysts, a typical characteristic peak of LaNiO$_3$ at 402 cm^{-1} is observed during the OER. Unlike the LaNiO$_3$, LaNiFeCoCrO$_3$, and LaNiFeCoCrMnO$_3$ catalysts, the characteristic peak of LaNiO$_3$ for S-LaNiFeCoCrMnO$_3$ catalyst is absent, suggesting that the existence of the sulfurized layer on

Open Access Article. Published on 17 2025. Downloaded on 23/09/25 16:31:42.
This article is licensed under a Creative Commons Attribution 3.0 Unported Licence.

Chemical Science Accepted Manuscript

View Article Online
DOI: 10.1039/D5SC04511

Open Access Article. Published on 17 2025. Downloaded on 23/09/25 16:31:42.
This article is licensed under a Creative Commons Attribution 3.0 Unported Licence.

Chemical Science Accepted Manuscript

S-La(NiFeCoMnCr)O_3 surface buries the signal of $LaNiO_3$. Besides, two peaks at 472 and 542 cm^{-1}, assigned to γ-NiOOH with NiO_2 subunit layer, respectively, appeared on $LaNiFeCoCrO_3$ and $LaNiFeCoCrMnO_3$ catalysts until the potential of 1.53 V *vs*. RHE was applied.[31] However, the peaks of γ-NiOOH didn't appear on $LaNiO_3$. Further, the emergence of the peaks for γ-NiOOH on S-La(NiFeCoMnCr)O_3 (1.33 V) is much earlier than on $LaNiFeCoCrO_3$ and $LaNiFeCoCrMnO_3$ catalysts. This result suggests that the existence of the sulfurized layer accelerates the surface reconstruction and facilitates the formation of γ-NiOOH active phase with NiO_2 subunit layer, thus enhancing the reactivity of lattice oxygen toward the OER. Coupling the *in situ* Raman spectra and HAADF-STEM results, it is proposed that the *in situ* formed Fe-NiOOH with NiO_2 subunit layer during the OER is the catalytic active phase toward the OER.[32]

XPS spectra of Ni 2p for $LaNiO_3$, $LaNiFeCoCrO_3$, $LaNiFeCoCrMnO_3$, and S-$LaNiFeCoCrMnO_3$ catalysts after stability test in **Fig. 3e** shows that the binding energies of Ni^{3+} $2p_{3/2}$ and Ni^{3+} $2p_{1/2}$ located at 854.4 eV and 865.7 eV, respectively. In **Fig. 3f**, there are two obvious peaks at 715.0 eV and 726.2 eV, which are attributed to the binding energy of Fe^{3+} $2p_{3/2}$ and Fe^{3+} $2p_{1/2}$, respectively. As the increase of elements/entropy in the perovskite of four perovskites, the binding energies of Ni^{3+} $2p_{3/2}$ exhibit the positive shift trend in the order of $LaNiO_3$, $LaNiFeCoCrO_3$, $LaNiFeCoCrMnO_3$, and S-$LaNiFeCoCrMnO_3$ after stability test. Whereas, the binding energies of Fe^{3+} $2p_{3/2}$ exhibit the negative shift trend in the order of $LaNiFeCoCrO_3$, $LaNiFeCoCrMnO_3$, and S-$LaNiFeCoCrMnO_3$ after stability test. Furthermore, the binding energies of Co^{3+} $2p_{3/2}$, Cr^{3+} $2p_{3/2}$, and Mn^{3+} $2p_{3/2}$ also display a decreased trend with the increase of elements in $LaNiFeCoCrO_3$, $LaNiFeCoCrMnO_3$, and S-$LaNiFeCoCrMnO_3$ catalysts (**Fig. S25**). This result indicates the strong electron transfer between Ni as the electron donator and Fe, Co, Cr, and Mn as the electron acceptor in S-$LaNiFeCoCrMnO_3$ facilitates the generation of high-valent Ni for *in situ* formed Fe-NiOOH during the OER.[33] CV curves of the catalysts in **Fig. S26** exhibit that the S-$LaNiFeCoCrMnO_3$ possesses more positive potential of Ni^{3+}/Ni^{4+} redox peaks (1.351 V) compared with that of $LaNiO_3$ (1.263 V), $LaNiFeCoCrO_3$ (1.282 V), and $LaNiFeCoCrMnO_3$ (1.319 V), demonstrating the formation of high-valent Ni^{4+} species in NiOOH active phase, formed on reconstructed S-$LaNiFeCoCrMnO_3$ during the OER because the existence of the sulfurized layer on S-$LaNiFeCoMnCrO_3$ surface promotes the surface reconstruction.[34,35] Therefore, we demonstrate that the *in situ* formed Fe-NiOOH active phase with NiO_2 subunit layer on reconstructed S-$LaNiFeCoMnCrO_3$ catalyst possesses high-valent Ni^{4+} species. The high-valent Ni^{4+} in S-$LaNiFeCoCrMnO_3$ also further results in the reduction of the covalency of Ni-oxygen bond, thus reinforcing the reactivity of lattice oxygen in the LOM.[36]

Mechanism insight of OER on S-$LaNiFeCoCrMnO_3$ for OER

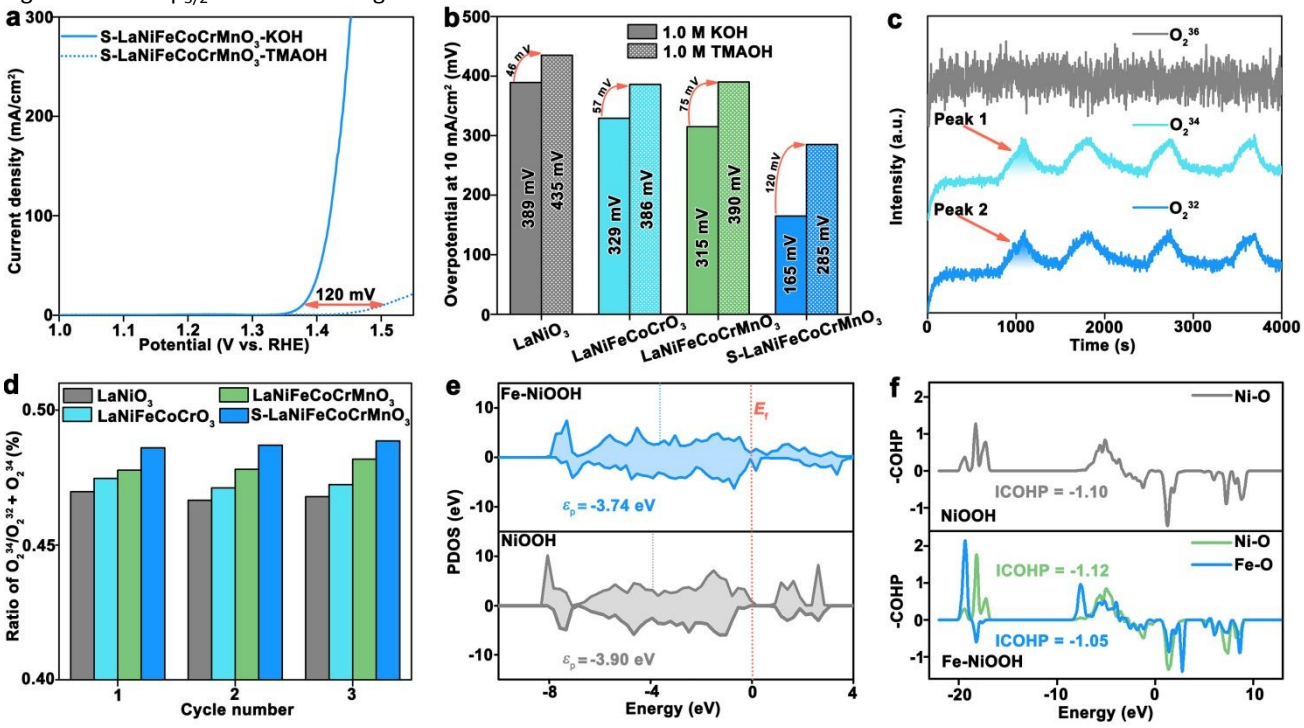

Fig. 4 Expounding LOM for S-$LaNiFeCoCrMnO_3$ catalyst toward the OER. (a) LSV curves of S-$LaNiFeCoCrMnO_3$ catalyst in 1.0 M KOH and 1.0 M TMAOH. (b) Overpotential comparison of $LaNiO_3$, $LaNiFeCoCrO_3$, $LaNiFeCoCrMnO_3$, and S-$LaNiFeCoCrMnO_3$ catalysts in 1.0 M KOH and 1.0 M TMAOH. (c) DEMS signals of O_2 products for ^{18}O-labeled S-$LaNiFeCoCrMnO_3$ catalyst in 1.0 M KOH with $H_2{}^{16}O$. (d) Comparison of peak area ratio of $^{34}O_2/(^{34}O_2 + {}^{32}O_2)$ for $LaNiO_3$, $LaNiFeCoCrO_3$, $LaNiFeCoCrMnO_3$, and S-

This journal is © The Royal Society of Chemistry 20xx

Please do not adjust margins

LaNiFeCoCrMnO$_3$ catalysts. (e) PDOS of lattice O atoms in NiOOH and Fe-NiOOH. (f) COHP plots of Ni-O bond for NiOOH and Fe-O and Ni-O bonds Fe-NiOOH.

View Article Online
DOI: 10.1039/D5SC04541J

In general, OER mechanism mainly includes adsorbate evolution mechanism (AEM) pathway and lattice oxygen mechanism (LOM) pathway. The AEM undergoes four concerted proton-electron transfer steps (CPET) occurring on metal site, while the LOM proceeds the non-concerted proton-electron transfer process. Unlike the AEM pathway, the O_2^{2-} forms for the LOM pathway during the OER. Therefore, the detection of O_2^{2-} species during the OER can effectively identify the reactivity of lattice oxygen for the LOM. The catalytic activity of catalyst and corresponding kinetics toward the OER would reduce when tetramethylammonium cation (TMA^+) attacks the O_2^{2-} species. As shown in **Fig. 4a**, S-LaNiFeCoCrMnO$_3$ catalyst exhibits significantly decreased OER overpotential in TMAOH solution than in KOH solution at 10 mA/cm^2. The difference of overpotential in 1.0 M TMAOH and 1.0 M KOH for S-LaNiFeCoCrMnO$_3$ (120 mV) is higher than that of LaNiO$_3$ (46 mV), LaNiFeCoCrO$_3$ (57 mV), and LaNiFeCoCrMnO$_3$ (75 mV), suggesting the enhanced reactivity of lattice oxygen for S-LaNiFeCoCrMnO$_3$ (**Fig. 4b** and **Fig. S27**).[37]

To further evaluate the reactivity of lattice oxygen for S-LaNiFeCoCrMnO$_3$, *on line* differential electrochemical mass spectrometry (DEMS) experiments were measured in 1.0 M KOH solution with $H_2{}^{16}O$ by using ^{18}O isotope-labeled catalysts, including LaNiO$_3$, LaNiFeCoCrO$_3$, LaNiFeCoCrMnO$_3$, and S-LaNiFeCoCrMnO$_3$ (**Fig. S28**). The DEMS results in **Fig. 4c** and **Fig. S29** reveal that the signals of O_2^{32} and O_2^{34} were detected, suggesting the generation of $O^{18}O^{16}$ species during the OER. Simultaneously, this result also further identifies that they follow the LOM. In addition, the ratio of O_2^{34} to O_2^{32} shows an increased trend in the order of LaNiO$_3$, LaNiFeCoCrO$_3$, LaNiFeCoCrMnO$_3$, and S-LaNiFeCoCrMnO$_3$, implying the lattice oxygen in S-LaNiFeCoCrMnO$_3$ catalyst more actively participated in OER process (**Fig. 4d**).[38]

DFT calculations were employed to investigate reaction mechanisms and activity origin. The Fe-NiOOH and NiOOH models were constructed to simulate the surface active phase on reconstructed S-LaNiFeCoCrMnO$_3$ and LaNiO$_3$ toward the OER (**Fig. S30**). Partial density of states (PDOS) results of lattice O atoms in **Fig. 4e** displayed that 2*p* orbitals of O atoms for Fe-NiOOH have a higher *p*-band center (ε_p) (-3.74 eV) than NiOOH (-3.90 eV), indicative of a higher lattice O activity, thereby enhancing the ratio of LOM during OER.[39-43] Furthermore, integrated crystal orbital overlap population (ICOHP) of Fe-O bonds in Fe-NiOOH (-1.05) was more positive than that of Ni-O bonds in Fe-NiOOH (-1.12) and NiOOH (-1.10), indicating the weakened Fe-O bonds and strong Ni-O bonds (**Fig. 4f**).[44] Hence, the introduction of Fe component enhances the Ni-O covalent bond, thereby promoting the activity of lattice oxygen in Fe-NiOOH. Electron localization function (ELF) of Fe-NiOOH and NiOOH was further calculated to investigate the covalency of Ni-O and Fe-O bonds. As shown in **Fig. S31**, Ni-O bonds in NiOOH have an ELF value of 0.72, while Ni-O bonds in Fe-NiOOH possess ELF values of 0.83, respectively. An ELF closer to 1 means a stronger covalency. Hence, the introduction of Fe in Fe-NiOOH active phase enhances the Ni-O covalent bond, thereby promoting the lattice O activity.[45]

Investigating atomic structure information for reconstructed S-LaNiFeCoCrMnO$_3$

X-ray absorption near-edge structure (XANES) was further used to investigate the structural and valency state change of reconstructed LaNiO$_3$, LaNiFeCoCrO$_3$, LaNiFeCoCrMnO$_3$, and S-LaNiFeCoCrMnO$_3$ catalysts after stability test. As shown in **Fig. 5a**, the Fe-edge XANES spectra show that the adsorption edge position exhibits a decreased trend in the order of reconstructed LaNiFeCoCrO$_3$, LaNiFeCoCrMnO$_3$, and S-LaNiFeCoCrMnO$_3$. This demonstrates that the valency state of Fe in reconstructed S-LaNiFeCoCrMnO$_3$ is lower than that of reconstructed LaNiFeCoCrO$_3$ and LaNiFeCoCrMnO$_3$, even if the Fe-NiOOH *in situ* formed on the catalyst surface.[46] The Ni K-edge XANES spectra of reconstructed LaNiO$_3$, LaNiFeCoCrO$_3$, LaNiFeCoCrMnO$_3$, and S-LaNiFeCoCrMnO$_3$ after stability test were shown in **Fig. 5b**. The white-edge energy position of Ni K-edge for S-LaNiFeCoCrMnO$_3$ after stability test is lower than that for LaNiO$_3$, LaNiFeCoCrO$_3$, and LaNiFeCoCrMnO$_3$. This result demonstrates that the oxidation state for Ni species of reconstructed S-LaNiFeCoCrMnO$_3$ after stability test is much closer to NiOOH compared with that of reconstructed LaNiO$_3$, LaNiFeCoCrO$_3$, and LaNiFeCoCrMnO$_3$, indicating the formation of a higher Ni oxidation state.

As shown in **Fig. 5c**, the average Ni oxidation state of reconstructed LaNiO$_3$, LaNiFeCoCrO$_3$, LaNiFeCoCrMnO$_3$, and S-LaNiFeCoCrMnO$_3$ exhibits an increased trend, while the average Fe oxidation state of reconstructed LaNiFeCoCrO$_3$, LaNiFeCoCrMnO$_3$, and S-LaNiFeCoCrMnO$_3$ exhibits a decreased trend. This result demonstrates that the Ni and Fe acted as the electron donor and acceptor in the *in situ* formed Fe-NiOOH on catalyst surface after OER, respectively, promoting the electron transfer and the formation of Ni active site with high valency. Fourier-transformed XANES (FT-XANES) spectra in **Fig. 5d** exhibit two dominant peaks at 1.44 Å and 2.57 Å, assigned to the Fe-O bond and Fe-Fe bond, respectively.[47] The shrinkable Fe-O bond length of S-LaNiFeCoCrMnO$_3$ compared with LaNiO$_3$, LaNiFeCoCrO$_3$, and LaNiFeCoCrMnO$_3$ indicates the increased metal-oxygen bond covalency, enhancing the stability of lattice oxygen during the OER (**Fig. S32**).[48] The wavelet-transformed (WT) XANES (WT-XANES) analysis results further support the above FT-XANES result (**Figs. S33-34**). The fitted data of FT-XANES reveals that the coordinate number (CN) of Fe-O bond for reconstructed S-LaNiFeCoCrMnO$_3$ is significantly higher than that of reconstructed LaNiFeCoCrO$_3$ and LaNiFeCoCrMnO$_3$ catalysts, indicating that it possesses more space for adsorbing the oxygen-containing intermediates and further enhancing the catalytic performance (**Fig. S33** and **Table S3**).[27]

Open Access Article. Published on 17 2025. Downloaded on 23/09/25 16:31:42.
This article is licensed under a Creative Commons Attribution 3.0 Unported Licence.

Chemical Science Accepted Manuscript

Please do not adjust margins

View Article Online
DOI: 10.1039/D5SC04541J

Open Access Article. Published on 17 2025. Downloaded on 23/09/25 16:31:42.
This article is licensed under a Creative Commons Attribution 3.0 Unported Licence.

Chemical Science Accepted Manuscript

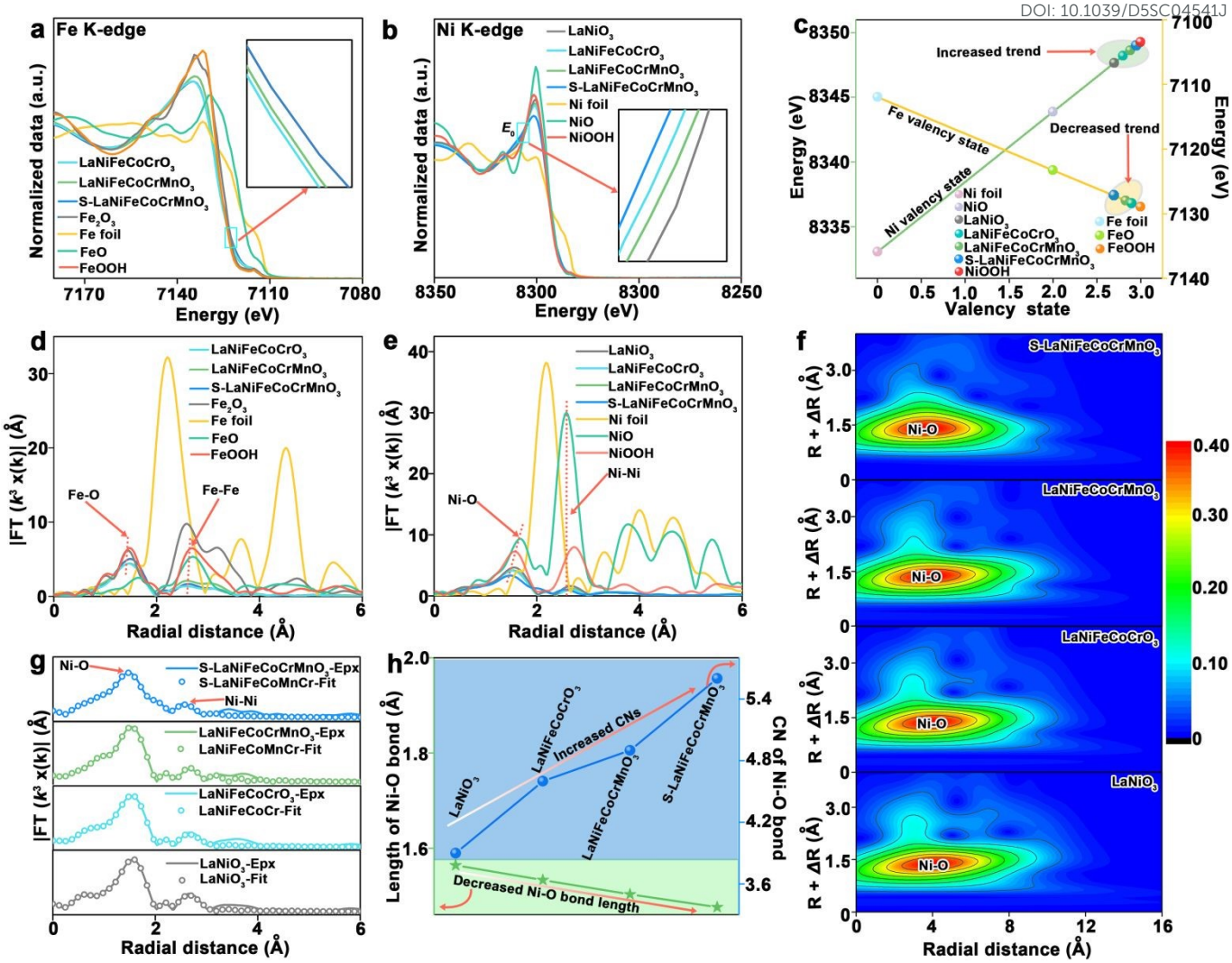

Fig. 5 (a) Fe K-edge XANES of $LaNiFeCoCrO_3$, $LaNiFeCoCrMnO_3$, and S-$LaNiFeCoCrMnO_3$ catalysts after stability test, and Fe foil, FeO, Fe_2O_3, and FeOOH act as the reference samples. (b) Ni K-edge XANES of $LaNiO_3$, $LaNiFeCoCrO_3$, $LaNiFeCoCrMnO_3$, and S-$LaNiFeCoCrMnO_3$ catalysts after stability test, and Ni foil, NiO, and NiOOH act as the reference samples. (c) Valence information of $LaNiO_3$, $LaNiFeCoCrO_3$, $LaNiFeCoCrMnO_3$, and S-$LaNiFeCoCrMnO_3$ catalysts after stability test. (d) Fe K-edge FT-XANES of $LaNiFeCoCrO_3$, $LaNiFeCoCrMnO_3$, and S-$LaNiFeCoCrMnO_3$ catalysts after stability test, and Fe foil FeO, Fe_2O_3, and FeOOH act as the reference samples. (e) Ni K-edge FT-XANES of $LaNiO_3$, $LaNiFeCoCrO_3$, $LaNiFeCoCrMnO_3$, and S-$LaNiFeCoCrMnO_3$ catalysts after stability test, and Ni foil, NiO, and NiOOH act as the reference samples. (f) Ni K-edge WT-XANES of $LaNiO_3$, $LaNiFeCoCrO_3$, $LaNiFeCoCrMnO_3$, and S-$LaNiFeCoCrMnO_3$ catalysts after stability test. (g) Fitting data of Ni K-edge FT-XANES of $LaNiO_3$, $LaNiFeCoCrO_3$, $LaNiFeCoCrMnO_3$, and S-$LaNiFeCoCrMnO_3$ catalysts after stability test. (h) Variational trend of Ni-O bond CNs and length for $LaNiO_3$, $LaNiFeCoCrO_3$, $LaNiFeCoCrMnO_3$, and S-$LaNiFeCoCrMnO_3$ catalysts after stability test.

FT-XANES spectra show that the Ni-O (1.58 Å) and Ni-Ni (2.73 Å) bonds were observed on the $LaNiO_3$, $LaNiFeCoCrO_3$, $LaNiFeCoCrMnO_3$, and S-$LaNiFeCoCrMnO_3$ (**Fig. 5e**).[49] The WT-XANES analysis result is consistent with the above FT-XANES results (**Fig. 5f**). Noting the significant elongate in Ni-O bond length of reconstructed S-$LaNiFeCoCrMnO_3$ compared with that of reconstructed $LaNiO_3$, $LaNiFeCoCrO_3$, and $LaNiFeCoCrMnO_3$ suggests the reduced metal-O covalency, thus reinforcing the reactivity of lattice oxygen around the Ni site in the *in situ* formed Fe-NiOOH during the OER (**Fig. 5g**). Besides, XANES spectra of Ni, Co, and Fe K-edge reveal that the Ni-S bond rather than Fe-S and Co-S bond was observed before the OER, suggesting that the S atoms coordinated with the Ni atoms on S-$LaNiFeCoCrMnO_3$ catalyst surface (**Figs. S35-37** and **Tables S4-S6**). Whereas, the intensity of Ni-S bond for S-$LaNiFeCoCrMnO_3$ reduced after the OER, which is consistent with ICP-OES result (**Fig. S17**). This result can infer that the existence of Ni-S bond in S-$LaNiFeCoCrMnO_3$ facilitates the surface reconstruction for *in situ* formation of Fe-NiOOH active phase during the OER. Further, as the number of doped elements for origin perovskite is increased, the Ni-O bond length and coordinate number (CNs) exhibit the decreased and increased trend in the order of $LaNiO_3$, $LaNiFeCoCrO_3$, $LaNiFeCoCrMnO_3$, and S-$LaNiFeCoCrMnO_3$ after stability test

This journal is © The Royal Society of Chemistry 20xx

Please do not adjust margins

View Article Online
DOI: 10.1039/D5SC04541J

for the OER, respectively (**Fig. 5h**, **Fig. S38**, and **Table S7**). The high CNs of Ni-O bond in S-LaNiFeCoCrMnO$_3$ after the OER implies that the *in situ* formed Fe-NiOOH on the catalyst surface could provide more space to bind oxygen-containing intermediates for improving the OER activity. Furthermore, CNs and length of Ni-O bond for LaNiO$_3$, LaNiFeCoCrO$_3$, LaNiFeCoCrMnO$_3$, and S-LaNiFeCoCrMnO$_3$ after stability test is close to NiOOH reference rather than NiO, further demonstrating the *in situ* formation of Fe-NiOOH active phase. Therefore, from the above XANES result, we can summarize the following points: (i) S atoms, which mainly coordinated with Ni atom to form Ni-S bond in the S-LaNiFeCoCrMnO$_3$ pre-catalyst, are partially leached, increasing coordinate numbers (CNs) of Ni-O bond, promoting the adsorption of the oxygen-containing intermediates, and thus facilitating the surface reconstruction of pre-catalyst during the OER to *in situ* form Fe-NiOOH active phase with NiO$_2$ subunit layer and Ni^{4+} species. Ni as the electron donator and Fe, Co, Cr, and Mn as the electron acceptor in S-LaNiFeCoCrMnO$_3$ pre-catalyst facilitates the generation of high-valent Ni^{4+} for *in situ* formed Fe-NiOOH with NiO$_2$ layer during OER.; (ii) the reduced Ni-O bond length implies that the reactivity of lattice oxygen located around the Ni sites was activated, while the enhanced Fe-O bond length means that the lattice oxygen near the Fe was stabilized for S-LaNiFeCoCrMnO$_3$. The activation and stability of lattice oxygen of reconstructed S-LaNiFeCoCrMnO$_3$ for the OER achieve a balance, thus breaking the trade-off relationship between activity and stability for the LOM toward the OER. (iii) The increased CNs of Fe-O and Ni-O for S-LaNiFeCoCrMnO$_3$ indicate that adsorption of the oxygen-containing intermediates was facilitated, which is an indication of favoring the enhancement of OER activity.

Conclusions

We have synthesized high-entropy S-LaNiFeCoCrMnO$_3$ catalyst, and it exhibited excellent catalytic performance for the OER in AEMWE. The existence of local Ni-S bonds in the sulfurized layer on S-LaNiFeCoMnCrO$_3$ surface faciliated *in situ* formation of Fe-NiOOH active phase with NiO$_2$ subunit layer and high-valent Ni^{4+}, enhancing the reactivity of lattice oxygen and improving LOM for OER. Such weak covalent Ni-O bonds and strong covalent Fe-O bonds in Fe-NiOOH active phase play the crucial role for increasing the reactivity and stability of lattice oxygen, respectively, thus breaking activity-stability trade-off and further improving the catalytic performance toward the OER. This work not only presents a highly active and stable catalyst for the OER at the anode in the AEMWE, but also deepens the understanding of lattice oxygen mechanism to optimize the catalytic performance toward the OER.

Author Contributions

G. Wang and Z. Li conceived the project and revised the manuscript. X. Li, Z. Li, B. Chen, and M. Wang conducted the material synthesis and material characterization. C. Yan and Z. Li conducted the TEM and HRTEM measurements. X. Li and Z. Li conducted the electrochemical measurements. Z. Li, S. Jane, and Q. Li conducted the XANES measurement. Z. Li, X. Li, Z. Liao, X. Meng and D. Gao completed the measurement of anion exchange membrane water electrolyzer. All authors contributed to the manuscript.

Conflicts of interest

The authors declare no competing financial interest.

Acknowledgements

This research work was supported by the National Key R&D Program of China (2022YFA1504001), the National Natural Science Foundation of China (22209172, 22125205, 22321002, U24A20499, 22494711 and 22350710789), the Strategic Priority Research Program of the Chinese Academy of Sciences (XDB0600200), the Liaoning Binhai Laboratory (LBLF-2023-02), the Fundamental Research Funds for the Central Universities (20720220008), the Yanchang Petroleum Group (yc-hw-2023ky-08). We thank staff at the BL14W1 beamline of the Shanghai Synchrotron Radiation Facility (SSRF) for their technical assistance during the XAFS measurements. We also acknowledge the Photon Science Center for Carbon Neutrality (JZHKYPT-2021-07).

References

[1] L. Quan, H. Jiang, G. Mei, Y. Sun, B. You, *Chem. Rev.*, 2024, **124**, 3694-3812.
[2] A. Vilanova, P. Dias, T. Lopes, A. Mendes, *Chem. Soc. Rev.*, 2024, **53**, 2388-2434.
[3] Y. Li, H. Zhou, S. Cai, D. Prabhakaran, W. Niu, A. Large, G. Held, R. A. Taylor, X.-P. Wu, S. C. E. Tsang, *Nat. Catal.*, 2024, **7**, 77-88.
[4] R. Ram, L. Xia, H. Benzidi, A. Guha, V. Golovanova, A. G. Manjón, D. L. Rauret, P. S. Berman, M. Dimitropoulos, B. Mundet, E. Pastor, V. Celorrio, C. A. Mesa, A. M. Das, A. Pinilla-Sánchez, S. Giménez, J. Arbiol, N. López, F. Pelayo García de Arquer, *Science* 2024, **384**, 1373–1380.
[5] Y. Yang, P. Li, X. Zheng, W. Sun, S. X. Dou, T. Ma, H. Pan, *Chem. Soc. Rev.*, 2022, **51**, 9620-9693.
[6] X. Liu, S. Wei, S. Cao, Y. Zhang, W. Xue, Y. Wang, G. Liu, J. Li, *Adv. Mater.*, **2024**, **36**, e2405970.
[7] Y. Yao, G. Zhao, X. Guo, P. Xiong, Z. Xu, L. Zhang, C. Chen, C. Xu, T. S. Wu, Y. L. S oo, Z. Cui, M. M. Li, Y. Zhu, *J. Am. Chem. Soc.*, 2024, **146**, 15219-15229.
[8] X. Yang, L. C. Elrod, T. Le, V. S. Vega, H. Naumann, Y. Rezenom, J. H. Reibenspies, M. B. Hall, M. Y. Darensbourg, *J. Am. Chem. Soc.* 2019, **141**, 15338−15347 3416.
[9] C. Liu, J. Qian, Y. Ye, H. Zhou, C.-J. Sun, C. Sheehan, Z. Zhang, G. Wan, Y.-S. Liu, J. Guo, S. Li, H. Shin, S. Hwang, T. B. Gunnoe, W. A. Goddard, S. Zhang, *Nat. Catal.*, 2020, **4**, 36-45.
[10] Y. Hao, S. F. Hung, W. J. Zeng, Y. Wang, C. Zhang, C. H. Kuo, L. Wang, S. Zhao, Y. Zhang, H. Y. Chen, S. Peng, *J. Am. Chem. Soc.*, 2023, **145**, 23659-23669.
[11] J. Huang, B. Hu, J. Meng, T. Meng, W. Liu, Y. Guan, L. Jin, X. Zhang, *Energy Evniron. Sci.* 2024, **17**, 1007

Open Access Article. Published on 17 2025. Downloaded on 23/09/25 16:31:42.
This article is licensed under a Creative Commons Attribution 3.0 Unported Licence.

Chemical Science Accepted Manuscript

Please do not adjust margins

View Article Online
DOI: 10.1039/D5SC04541J

Open Access Article. Published on 17 2025. Downloaded on 23/09/25 16:31:42.
This article is licensed under a Creative Commons Attribution 3.0 Unported Licence.

Chemical Science Accepted Manuscript

[12] H. Zhao, L. Zhu, J. Yin, J. Jin, X. Du, L. Tan, Y. Peng, P. Xi, C. H. Yan, *Angew. Chem.*, *Int. Ed.*, 2024, **63**, e202402171.

[13] Y. Sun, Y. Zhao, X. Deng, D. Dai, H. Gao, *Sustainable Energy Fuels* 2022, **6**, 1345-1352.

[14] G. Choi, U. Chang, J. Lee, K. Park, H. Kwon, H. Lee, Y.-I. Kim, J. H. Seo, Y.-C. Park, I. Park, J. Kim, S. Lee, J. Choi, B. Yu, J.-H. Song, H. Shin, S.-W. Baek, S. K. Lee, H. Park, K. Jung, *Energy Environ. Sci.* 2024, **17**, 4634–4645.

[15] X. Liang, W. Yan, Y. Yu, K. Zhang, W. An, H. Chen, Y. Zou, X. Zhao, X. Zou, *Angew. Chem.*, *Int. Ed.*, 2023, **62**, e202311606.

[16] L. Tang, Y. Yang, H. Guo, Y. Wang, M. Wang, Z. Liu, G. Yang, X. Fu, Y. Luo, C. Jiang, Y. Zhao, Z. Shao, Y. Sun, *Adv. Funct. Mater.*, 2022, **32**, 2112157.

[17] X. Liang, Q. Wu, Q. Liu, L. Wang, M. Zhang, K. Sun, Y. Shen, H. Chen, X. Zou, *Energy Lab,* 2023, **1**, 220013.

[18] X. Ren, Y. Zhai, P. Wang, Z. Xu, S. Gao, X. Chen, Q. Gu, B. Wang, J. Li, S. F. Liu, *Adv. Mater.*, 2023, **35**, e2301166.

[19] X. Du, M. Qi, Y. Wang, *Acc. Chem. Res.* 2024, **57**, 1298−1309.

[20] Y. Tang, C. Wu, Q. Zhang, H. Zhong, A. Zou, J. Li, Y. Ma, H. An, Z. Yu, S. Xi, J. Xue, X. Wang, J. Wu, *Angew. Chem.*, *Int. Ed.*, 2023, **62**, e202309107.

[21] Y. Hu, Y. Zheng, J. Jin, Y. Wang, Y. Peng, J. Yin, W. Shen, Y. Hou, L. Zhu, L. An, M. Lu, P. Xi, C. H. Yan, *Nat. Commun.*, 2023, **14**, 1949.

[22] Z. Shao, Q. Zhu, Y. Sun, Y. Zhang, Y. L. Jiang, S. Q. Deng,W. Zhang, K. K. Huang, S. H. Feng, *Adv. Mater.* 2022, **34**, 2110172.

[23] H. Wu, Q. Lu, Y. Li, M. Zhao, J. Wang, Y. Li, J. Zhang, X. Zheng, X. Han, N. Zhao, J. Li, Y. Liu, Y. Deng, W. Hu, *J. Am. Chem. Soc.*, 2023, **145**, 1924-1935.

[24] Y. Yan, J. Lin, K. Huang, X. Zheng, L. Qiao, S. Liu, J. Cao, S. C. Jun, Y. Yamauchi, J. Qi, *J. Am. Chem. Soc.*, 2023, **145**, 24218-24229.

[25] Z. Li, Z. Xie, H. Chen, X. Liang, X. Ai, L. Yuan, X. Li, X. Zou, *Chem. Engin. J.*, 2021, **419**, 129568.

[26] Z. Li, L. Sheng, R. Deng, Z. Zheng, P. Hou, M. Chen, Z. Ma, K. Sun, Y. Wang, Q. Liu, P. Xu, X. Ma, H. Chu, *ACS Energy Lett.*, 2023, **8**, 5136-5142.

[27] Z. Li, X. Li, M. Wang, Q. Wang, P. Wei, S. Jana, Z. Liao, J. Yu, F. Lu, T. Liu, G. Wang, *Adv. Mater.*, **2024**, **36**, e2402643.

[28] Z. Y. Yu, Y. Duan, Y. Kong, X. L. Zhang, X. Y. Feng, Y. Chen, H. Wang, X. Yu, T. Ma, X. Zheng, J. Zhu, M. R. Gao, S. H. Yu, *J. Am. Chem. Soc.*, 2022, **144**, 13163-13173.

[29] Y. Wang, X. Ge, Q. Lu, W. Bai, C. Ye, Z. Shao, Y. Bu, *Nat. Commun.*, 2023, **14**, 6968.

[30] J. Cai, H. Zhang, L. Zhang, Y. Xiong, T. Ouyang, Z. Q. Liu, *Adv. Mater.*, 2023, **35**, e2303488.

[31] Y. Hao, Y. Li, J. Wu, L. Meng, J. Wang, C. Jia, T. Liu, X. Yang, Z. P. Liu, M. Gong, *J. Am. Chem. Soc.*, 2021, **143**, 1493-1502.

[32] X. Bai, M. Zhang, Y. Shen, X. Liang, W. Jiao, R. He, Y. Zou, H. Chen, X. Zou, *Adv. Funct. Mater.*, 2024, **34**, 2400979.

[33] C. Wu, X. Wang, Y. Tang, H. Zhong, X. Zhang, A. Zou, J. Zhu, C. Diao, S. Xi, J. Xue, J. Wu, *Angew. Chem.*, *Int. Ed.*, 2023, **62**, e202218599.

[34] Y.-N. Zhou, F.-T. Li, B. Dong, Y.-M. Chai, *Energy Environ. Sci*. 2024, **17**, 1468.

[35] N. Zhang, X. Feng, D. Rao, X. Deng, L. Cai, B. Qiu, R.Long, Y. Xiong, Y. Lu, Y. Chai, *Nat. Commun*. 2020, **11**, 4066.

[36] E. Gioria, S. Li, A. Mazheika, R. Naumann d'Alnoncourt,A. Thomas, F. Rosowski, Angew. Chem., Int. Ed. 2023, **62**,202217888.

[37] F. Wang, P. Zou, Y. Zhang, W. Pan, Y. Li, L. Liang, C. Chen, H. Liu, S. Zheng, *Nat. Commun.*, 2023, **14**, 6019

[38] C. Hu, K. Yue, J. Han, X. Liu, L. Liu, Q. Liu, Q. Kong, C.-W. Pao, Z.Hu, K. Suenaga, D. Su, Q. Zhang, X. Wang, Y. Tan, X. Huang, *Sci. Adv*. 2023, **9**, eadf9144.

[39] C. Wang, P. Zhai, M. Xia, W. Liu, J. Gao, L. Sun, J. Hou, *Adv. Mater.*, 2023, **35**, e2209307.

[40] X. Wang, S. Xi, P. Huang, Y. Du, H. Zhong, Q. Wang, A. Borgna, Y. W. Zhang, Z. Wang, H. Wang, Z. G. Yu, W. S. V. Lee, J. Xue, *Nature* 2022, **611**, 702-708.

[41] Q. Ji, B. Tang,X. Zhang, C. Wang, H. Tan, J. Zhao, R. Liu, M. Sun, H. Liu, C. Jiang,J. Zeng, X. Cai, W. Yan, *Nat. Commun*. 2024, **15**, 808.

[42] Z.-F. Huang, J. Song, Y. Du, S. Xi, S. Dou, J. M. V. Nsanzimana, C. Wang, Z. J. Xu, X. Wang, *Nat. Energy* 2019, **4**, 329-338.

[43] T. Wu, S. Sun, J. Song, S. Xi, Y. Du, B. Chen, W. A. Sasangka, H. Liao, C. L. Gan, G. G. Scherer, L. Zeng, H. Wang, H. Li, A. Grimaud, Z. J. Xu, *Nat. Catal*., 2019, **2**, 763-772

[44] J. Wei, Y. Shao, J. Xu, F. Yin, Z. Li, H. Qian, Y. Wei, L. Chang, Y. Han, J. Li and L. Gan, *Nat. Commun*., 2024, **15**, 9012.

[45] C. Cheng, C. Chen, S. Chu, H. Hu, T. Yan, X. Xia, X. Feng, J. Guo, D.Sun, J. Wu, S. Guo, L. Zhang, *Adv. Mater.* 2022, **34**, 2201152.

[46] S. Li, G. Wang, H. Lv, Z. Lin, J. Liang, X. Liu, Y. G. Wang, Y. Huang, G. Wang, Q. Li, *J. Am. Chem. Soc.* 2024, **146**, 17659−17668.

[47] D. Friebel, M. W. Louie, M. Bajdich, K. E. Sanwald, Y. Cai, A. M. Wise, M. J. Cheng, D. Sokaras, T. C. Weng, R. Alonso-Mori, R. C. Davis, J. R. Bargar, J. K. Norskov, A. Nilsson, A. T. Bell, *J. Am. Chem. Soc.*, 2015, **137**, 1305-1313.

[48] H. Gao, Z. Xiao, S. Du, T. Liu, Y. C. Huang, J. Shi, Y. Zhu, G. Huang, B. Zhou, Y. He, C. L. Dong, Y. Li, R. Chen, S. Wang, *Angew. Chem.*, *Int. Ed.*, 2023, **62**, e202313954.

[49] Y. Zhao, Q. Wen, D. Huang, C. Jiao, Y. Liu, Y. Liu, J. Fang, M. Sun, L. Yu, *Adv. Funct. Mater.*, 2023, **13**, 2203595.

This journal is © The Royal Society of Chemistry 20xx

View Article Online
DOI: 10.1039/D5SC04541J

The data supporting this article have been included as part of the Supplementary Information.

Open Access Article. Published on 17 2025. Downloaded on 23/09/25 16:31:42.
This article is licensed under a Creative Commons Attribution 3.0 Unported Licence.

Chemical Science Accepted Manuscript